JTTEE5 17:244–253
DOI: 10.1007/s11666-008-9166-4
1059-9630/$19.00 © ASM International

Microstructure and Creep Behavior of Plasma-Sprayed Yttria Stabilized Zirconia Thermal Barrier Coatings

Reza Soltani, Tom W. Coyle, and Javad Mostaghimi

(Submitted September 3, 2007; in revised form October 30, 2007)

The purpose of this study was to determine the creep/sintering characteristics of thermally sprayed zirconia coatings and attempt to understand the influence of microstructure on the creep resistance of deposits. The major modification, compared with more typical practice, was employment of a new powder feedstock with agglomerated sub-micron size particles (Nanox), which is compared to one of the best commercially available powders (HOSP). Thick plasma-sprayed coatings were prepared and their physical and mechanical properties were characterized. Creep/sintering experiments were then conducted to investigate the response of the materials when exposed to high temperatures under load. The results showed that it could be possible to correlate the splat thickness to the creep behavior of the coatings.

Keywords coating, creep, microstructure, plasma spray, thermal barrier, zirconia

1. Introduction

Thermal barrier coatings such as zirconia have been used to protect turbine blades and combustion chambers for many years (Ref 1-5). These coatings have been developed for a long while, but still the service life needs to be extended to longer lives and made more predictable. There are several mechanisms involved in reducing the life time of a coating but residual stresses due to thermal expansion mismatches between coating, bond coat and substrate play an important role.

The residual stresses may activate mechanisms such as crack initiation and propagation and creep at elevated temperatures. As the operating temperatures approach 1000 °C the presence of relatively high compressive stresses at the coating surface lead to stress relaxation by creep and/or sintering mechanisms due to heat transition under steady-state conditions. Shrinkage at high temperatures followed by crack initiation and propagation during cooling may cause spallation of the coating and reducing the life time of the deposit. Creep/sintering behavior of bulk and plasma-sprayed zirconia has been investigated by several researchers (Ref 1-10).

Reza Soltani and **Tom W. Coyle**, Department of Materials Science and Engineering, Centre for Advanced Coating Technologies, University of Toronto, Toronto, Ontario, Canada; **Javad Mostaghimi**, Department of Mechanical and Industrial Engineering, Centre for Advanced Coating Technologies, University of Toronto, Toronto, Ontario, Canada. Contact e-mail: rsoltani@mie.utoronto.ca.

In the current study microstructure of the partially stabilized zirconia (PSZ) coatings deposited by atmospheric plasma spraying was investigated and correlated to the creep behavior of the coating in high temperatures.

2. Experiments and Results

Two commercially available 6-8 wt.% Y_2O_3-PSZ powders were used to deposit coatings by air plasma spraying. Nanox powder consisted of agglomerates (Nanox S4007, Inframat Corp., CT) 15-150 μm in diameter made up of particles on the order of 200 nm in diameter and HOSP powder consisted of hollow spherical particles (204B-NS, Sulzer-Metco, NY) with particle size distribution of 45-75 μm; both were deposited with SG-100 (Praxair, Concord, NH) plasma torch.

A range of deposition parameters were employed to produce different microstructures for each of these feedstocks on carbon steel plates. The characteristic examinations revealed that the structure of both type of powders and coatings are made of tetragonal phase zirconia. The chemical compositions of the powders did not show any major differences either (Ref 11).

A Clemex image analyzer (Clemex Vision Professional, Clemex, QC, Canada) was used to determine the average porosity of each sample. Creep tests were conducted on free standing 3-mm-thick coatings (substrate was removed by dissolving in concentrated nitric acid) employing a SiC four-point bend test fixture enclosed in a resistance heated box furnace at elevated temperatures under a range of applied loads; as described elsewhere (Ref 12).

The creep tests were performed at 1000 °C under various stresses for 2 days. Four samples with different process parameters, listed in Table 1 were selected to produce thick samples. This selection makes it possible to

Table 1 In-flight properties of selected Nanox and HOSP coating showing the porosity and the volume fraction of non-melted particles

Sample	Powder	Velocity, m/sec	Temperature, °C	Diameter, μm	Image analysis, %	
					Porosity	Non-molten
A3	Nanox	179	3021	56	12 ± 1	4 ± 2
A4	Nanox	148	2958	52	12 ± 1	1.5 ± 1
A5	Nanox	130	2533	48	18 ± 1	4.5 ± 1
A8	HOSP	144	2809	56	11 ± 1	···

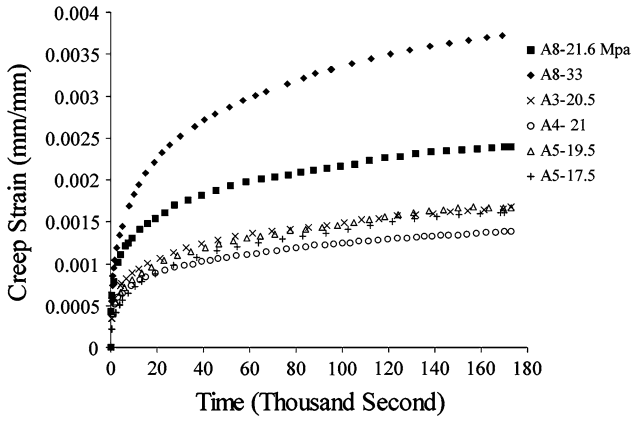

Fig. 1 Creep strain of Nanox and HOSP samples under a range of stresses at 1000 °C for 2 days

investigate the effect of porosity and non-melted particles on creep/sintering properties of Nanox and HOSP coatings in a comparable conditions: Nanox samples A3 and A4 having same porosity but different non-molted particles, Nanox sample A5 which has almost same non-melted particles as A3 but higher porosity level and finally HOSP sample A8 with total porosity similar to Nanox A3 and insignificant amount of non-melted particles. This selection was based on sample Nanox A5 which showed the lowest thermal diffusivity and conductivity among the rest of the other deposits (Ref 11). Analyzing creep results showed low activation energy of 154 and 190 KJ/mol for Nanox and 204B-NS, respectively, and stress exponent of about unit for both type of coatings indicating a diffusion mechanism involvement (Ref 11).

Figure 1 shows the creep results of selected samples at 1000 °C under a narrow range of stresses. This graphs shows that the creep resistance of Nanox coatings is relatively higher than HOSP deposits after being held at this temperature for 2 days. Creep test at different temperatures has revealed the same behavior (Ref 11).

3. Discussion

The creep tests illustrate no constant creep rates. All specimens showed a quasi steady-state behavior. The Nanox and HOSP samples kept at 1000 °C for more than 4 days showed no stationary creep stage either. It has been shown that plasma-sprayed zirconia coatings demonstrate a long-primary creep stage which is not only a function of temperature and stress but also is time dependent (Ref 13). This behavior, generally, can be expressed by the following equation (Ref 1):

$$\dot{\varepsilon} = A\left(\frac{\sigma^n}{D^p}\right)\exp\left(\frac{-Q}{RT}\right)t^{-s} \qquad \text{(Eq 1)}$$

where $\dot{\varepsilon}$ denotes creep rate (sec^{-1}), A material constant (Sec), σ normalized applied stress, n stress exponent, D grain size, p grain size exponent, Q apparent activation energy of creep (J/mol), R the gas constant (J/molK), T absolute temperature (K), t time, and s time exponent. Since the creep deformation could strongly be dependent on the constitution of the material, a structure term (S) is required in the creep equations which involves both ''macrostructure (i.e., grain size, porosity, phase distribution) and microstructure (i.e., crystal structure, point defects, dislocation tangles, vacancy clusters, etc.)'' (Ref 13):

$$\text{Creep Deformation} = \mathrm{f}(\sigma, t, T, S) \qquad \text{(Eq 2)}$$

3.1 Microstructures of the Nanox and HOSP coatings

In thermally sprayed structures, instead of particles, there are splats and columnar grains. In the Nanox coating, in addition to these conventional splats and grains, there are regions with another form of material made of sub-micron size particles (<200 nm). Figure 2 shows the columnar grains in fracture surface of as-sprayed HOSP coating and sub-micron size particles in as-sprayed Nanox coating.

In the absence of chemical reactions, reduction in surface area and relaxation of stresses may occur at elevated temperatures by solid-state diffusion. Changes in microstructure by diffusive processes, driven by the local differences in the surface curvature, are referred to as sintering. Among conventional splats this occurs in two regions: between splats and within splats, called splat joining and micro-crack healing, respectively. Figure 3 illustrates these two processes schematically. The process which leads to the bridging of inter-lamellar voids begins as grain boundary grooving; if the two splat surfaces are close enough, the roughly spherical caps which form on the top of the columnar grains may touch, forming a neck. The surface curvatures then lead to growth of the neck, joining the two columnar grains in a process analogous to

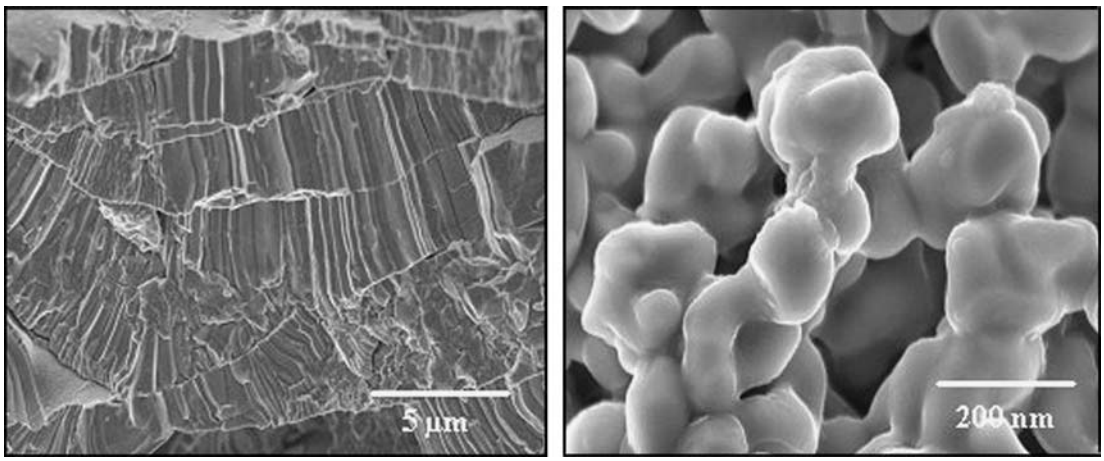

Fig. 2 Microstructure of a fractured as-sprayed HOSP coating (left) showing columnar grains and Nanox sub-micron size particles (right)

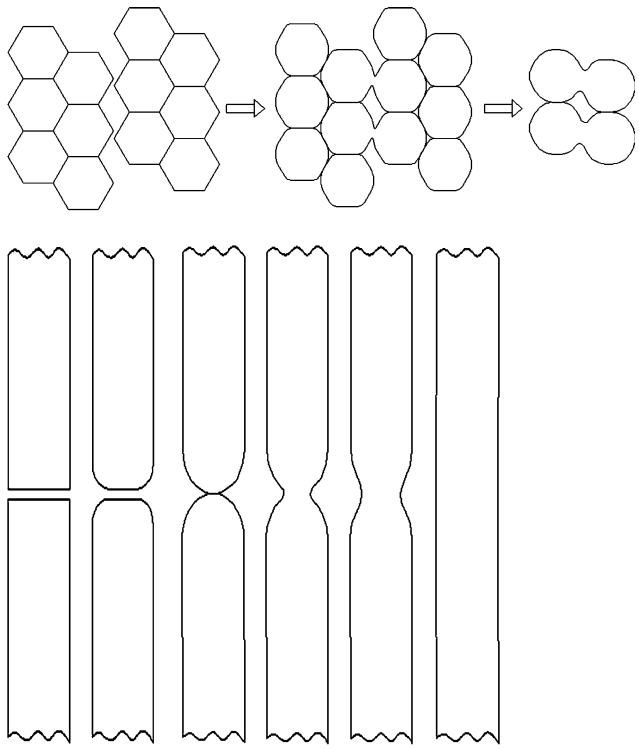

Fig. 3 Schematic diagram of sintering mechanisms; top: splat joining (inter-splat) and bottom: micro-crack healing (intra-splat) of thermally sprayed coatings

the sintering of powder particles. A similar scenario happens in healing of micro-cracks. The annihilation of the narrow intralamellar cracks in plasma-sprayed 7 wt.% YSZ after annealing at 1000 °C for 10 h was reported previously (Ref 1, 2, 14).

At relatively low temperatures (here 1000 °C), only defects with small gaps in between can be healed. This would include thin inter-lamellar pores or planar voids and micro-cracks. At higher temperatures, however, diffusion would occur considerably more rapidly and the healing of larger defects, like globular pores, becomes possible (Ref 15).

Figures 4 and 5 show SEM images of these sintering processes in HOSP and Nanox coatings produced in this study; after being tested for 2 days at 1000 °C under about 20 MPa bending stress in the four-point configuration. At this temperature the most dominant mass transport mechanism in zirconia is surface diffusion (Ref 16-18).

Grain boundary grooving and pore smoothing observations, as well as particle neck growth measurements in ZrO_2-3 mol% Y_2O_3, have been shown to be consistent with a surface diffusion mechanism. Evidence of Zr^{4+} ion transport to the neck between spherical powders was observed at temperatures from 870 to 1050 °C (Ref 19-20). In situ TEM experiments at 890 °C also noted surface diffusion was the likely transport mechanism for pore smoothing between nanocrystalline grains of zirconia (Ref 21).

Growth of the columnar grains inside the splats was not observed. The stability of this columnar structure is probably due to the very narrow range of grain diameters, which results in most boundaries meeting at triple points at angles very close to 120°. The non-molten sub-micron particles in Nanox coatings also start to sinter during the creep test. In spite of having very small size (<200 nm), which produces high surface curvatures and a good driving force for sintering, these particles are not sintered completely under the current test conditions. This is consistent with surface diffusion being the dominant mass transport mechanism, since this mechanism does not cause shrinkage, only coarsening of the necks (Fig. 6).

3.2 Microstructure and Creep

The chemical composition of the Nanox and HOSP samples shows that there are several uninvited constituents in their powder (Table 2). These materials may diffuse out of zirconia grains into the grain boundaries due to segregation processes. Generally, having a lower melting

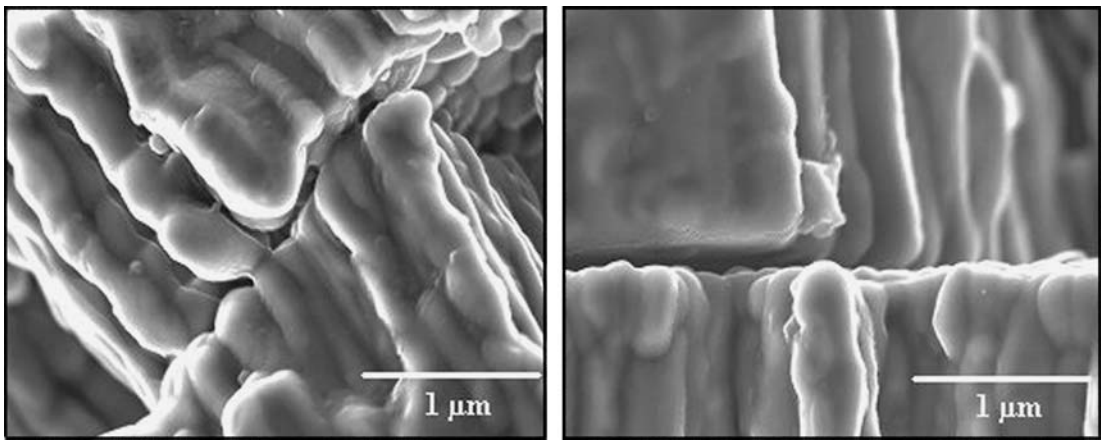

Fig. 4 SEM images of HOSP microstructure showing inter-splat sintering after being tested at 1000 °C under 20 MPa bending stress for 2 days

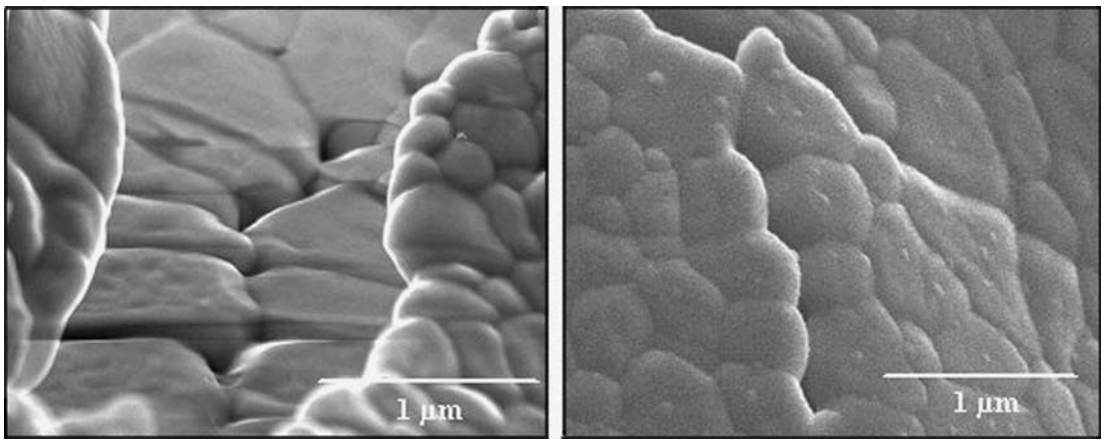

Fig. 5 SEM images of micro-crack healing of a Nanox sample crept at 1000 °C for 2 days under 20 MPa bending stress

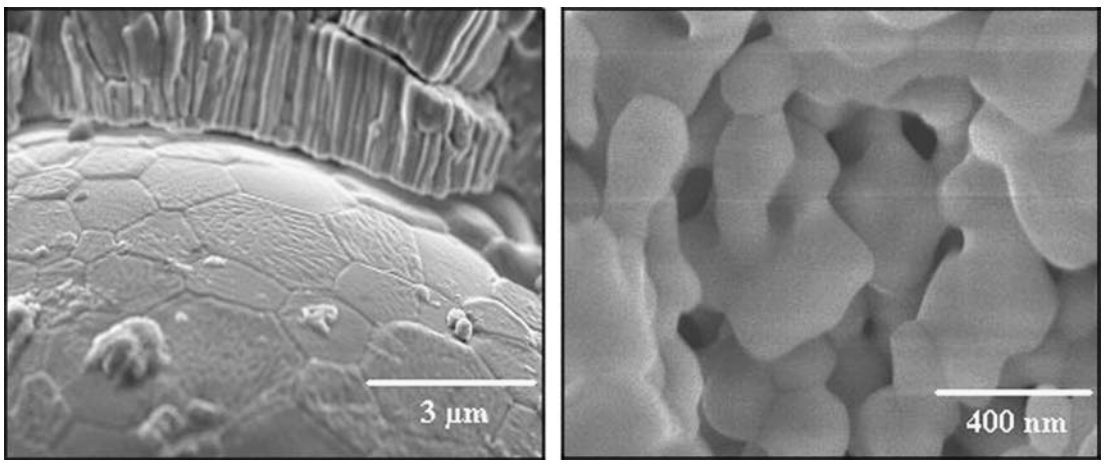

Fig. 6 SEM images of HOSP splat surfaces showing grain boundaries (left) and sub-micron size particles of Nanox coating after creep at 1000 °C for 2 days

point than zirconia, they may create glassy phases at elevated temperatures. The presence of such glassy phases at grain boundaries would dramatically increases the creep rate.

Since no significant differences between the chemical compositions of the two materials were found, if these constituents were to have any effect on the creep/sintering behavior of the samples, it is expected that it would be similar for both. To examine the possibility of any glassy phase's contribution to overall creep deformation, TEM (Transmission Electron Microscopy) and EDX (Energy Dispersive X-ray Spectroscopy) investigations were performed on coatings. Figure 7 shows TEM images of Nanox and HOSP splats. The EDX line scans were performed across inter-splat and columnar grain boundaries to detect possible segregation. Having no segregation in as-sprayed deposits could be due to rapid solidification of the plasma spray coating, which does not allow sufficient time for segregation to occur. Performing creep tests on the Nanox and HOSP coatings provides opportunity for diffusion of atoms. Therefore, the glassy phase might be present at elevated temperatures thus TEM investigation was conducted on crept samples. In as-sprayed specimens no sub-micron particles were observed, probably because of not being bonded to the structure strongly.

In crept samples, due to the sintering which has taken place for 2 days at 1000 °C, the sub-micron particles were held in the TEM specimens and visible in the images (Fig. 8). For crept samples, EDX line scans were also performed, but again no segregation was found at boundaries. EELS (Electron Energy Loss Spectroscopy) has a higher sensitivity for silica, the most common constituent of glassy phases at boundaries. Therefore, this technique was also employed to search for Si segregation. No segregation of Si was observed and it was concluded that no segregation has happened in samples during creep, therefore there was no contribution to deformation by viscous creep in the samples of this study.

In the absence of impurities segregation, similar chemical composition and lamella structure of the coatings, it could be concluded that the dissimilarity of microstructure between Nanox and HOSP coatings plays the key role in determining the creep resistance.

Table 1 shows the properties of in-flight particles of HOSP and Nanox powders. The major differences are the velocity and temperature of these particles. As these properties increase, the flattening ratio (diameter of a disk shape splat to the diameter of in-flight particle) increases if other parameters are kept similar (Ref 22). It means that the higher this ratio the thinner would be the splat thickness.

To investigate the possibility of splat thickness variations in Nanox and HOSP coatings and measure the average thicknesses, these two deposits were examined by three different techniques. These methods are: Empirical equations, computer simulations and SEM examinations. The thicknesses obtained from these methods will be compared and their consistency will be discussed in the following sections.

3.2.1 Analytical Model. In this method, the thickness of splats was measured by Eq. 3.

$$R_f = \alpha(\mathrm{Vp.Dp}/\nu)^{\beta} \quad \text{(Eq 3)}$$

where R_f is flattening ratio, Vp particle velocity, Dp particle diameter, ν kinematic viscosity, α, β, A, and B are all constants (Ref 22). The empirical constants and viscosity formula were obtained from the literature as: $\alpha = 0.83$ and $\beta = 0.2$ and $\mu = 0.0037\exp(6110/T)$ where μ is the viscosity in Kg/msec and T is the particle temperature in K. Then

Table 2 Chemical composition of the two feedstock powders; Nanox and HOSP

	Nanox, %	HOSP, %	Technique
Al_2O_3	0.66	0.66	ICP
CuO	0.007	0.008	ICP
CaO	0.025	0.026	ICP
Fe_2O_3	0.006	0.009	ICP
HfO_2	1.74	1.52	ICP
P_2O_5	0.04	0.04	ICP
SiO_2	0.12	0.11	ICP
TiO_2	0.06	0.14	ICP
Na_2O	0.03	0.02	FP
Y_2O_3	6.43	7.30	ICP

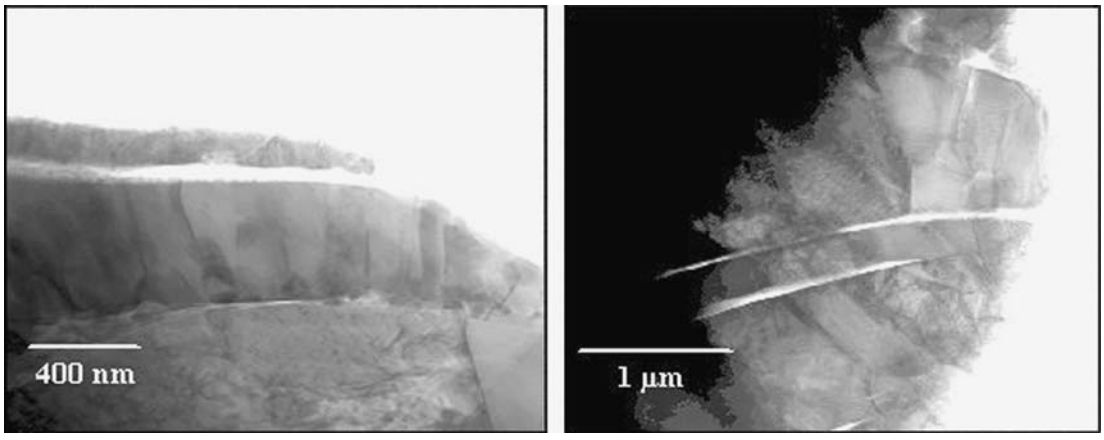

Fig. 7 TEM images of Nanox (left) and HOSP (right) coatings showing cross section of splats

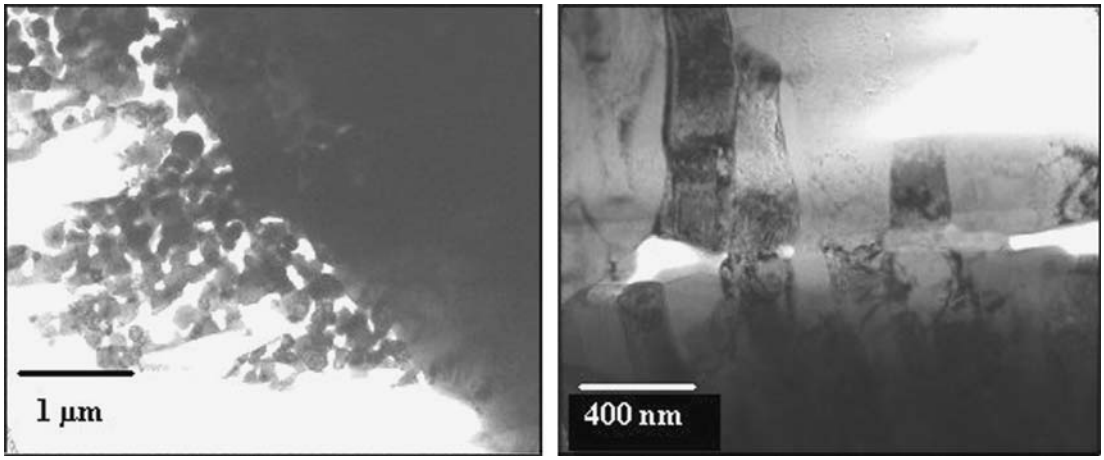

Fig. 8 TEM images of crept Nanox (left) and HOSP (right) coatings after 2 days at 1000 °C under 21 MPa bending stress

the in-flight properties of particles in Table 1 were used to calculate the flattening ratio; Table 3 shows the results of these calculations. As the velocity and temperature of in-flight particles increase, the flattening ratio is raised too and consequently the thickness of splat decreases. Table 3 shows the splat thicknesses of A3, A4, A5, and A8 coatings. The thickness of sample A8 is about 50% lower than that in A5 coating, while the creep strain of A5 is significantly lower than the A8 specimen.

Table 3 Flattening ratio and splat thicknesses of Nanox and HOSP coatings

Sample	Flattening ratio	Thickness, μm
A3	3.95	2.4
A4	3.73	2.6
A5	3.35	2.9
A8	2.94	1.9

The average diameter of in-flight particles is one of the parameters in Eq. 3, but since the diameter of in-flight particles fall into a very small range therefore they do not change the flattening ratio significantly.

3.2.2 Simulation. Computer simulations were performed based on the finite volume code developed in CACT (Centre for Advanced Coating Technologies, University of Toronto) accommodating in-flight particles data and material properties (Ref 23). Figure 9 shows the results of this simulation based on process parameters of Nanox A5 and HOSP A8 samples, indicating that the thickness of splats in Nanox coating is about 25% higher than that in HOSP splats; 3.6 and 2.7 μm for Nanox and HOSP splats, respectively. The absolute values of thickness obtained from this method is different from the experimental measurements, but still it shows 1-μm larger thickness for splats of Nanox coatings.

3.2.3 SEM Investigation. To observe and measure the actual splat thickness in coatings, extensive SEM investi-

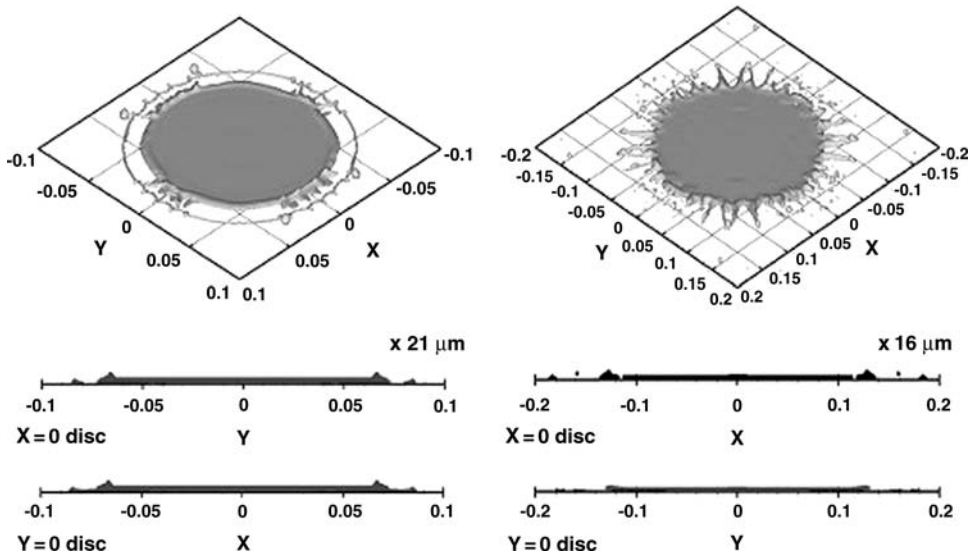

Fig. 9 Computer simulation of splat formation; Left: HOSP A8 with 2.7 μm and right: Nanox A5 with 3.6-μm central thickness

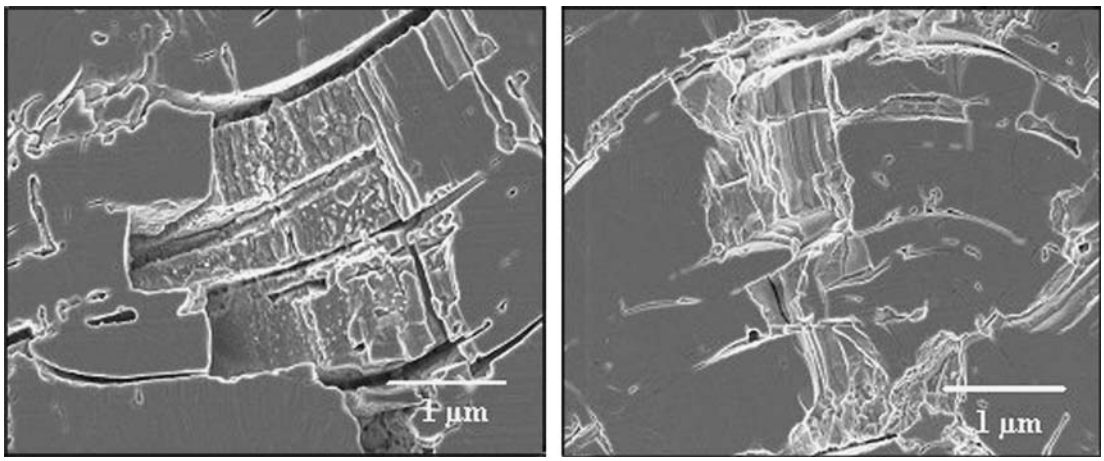

Fig. 10 Typical SEM images of Nanox (left) and HOSP (right) samples showing thickness of splats in chemically etched coatings

gation was conducted. To reveal the splat boundaries, the surface of samples either should be etched or fractured surfaces have to be examined. The accuracy of the former method to expose the thickness of splats depends drastically on the sample preparation (etching); if all the splat boundaries are not revealed by etching, then the measured thickness would be higher than the real values. Figure 10 clearly shows this problem. The broken surfaces reveal the splats boundaries beneath them, which illustrate the presence of thinner splats rather than thick ones. Therefore, the fractured surfaces were examined to determine the splat thickness. A total of 20 images were taken from each sample and the average thickness of splats in all images was calculated.

Results showed that splat thickness of Nanox A5 and HOSP A8 coatings are 2.8 ± 0.3 and 1.8 ± 0.2 µm, respectively. Again, measurement indicates that the thickness of splats in the Nanox sample is larger than that in HOSP deposit. These values are in good agreement with those obtained by analytical technique.

Results summary from these three techniques show higher splat thickness values for the Nanox coating. This reduction in splat thickness of HOSP sample A8 (~1 µm) would result in a consequent increase of about 25-30% in linear density of splat interfaces in a given thickness.

The significant primary creep phase and low apparent creep activation energy for plasma-sprayed coatings (as were observed in this study) are attributed to mechanical sliding and temperature and stress-enhanced diffusion along the splat boundaries (Ref 1). Therefore, the higher the density of the inter-splat boundaries the higher the creep strain.

The splat thickness for A8, A3, A4, and A5 coatings increases continuously (Table 3) and creep strain drops correspondingly. The only inconsistency is the Nanox A5 coating which has the thickest splat but the creep strain is slightly higher than Nanox A4 sample with thinner splats. Since the A5 specimen has the highest porosity level among the rest of samples (18% compared to 11 and 12%

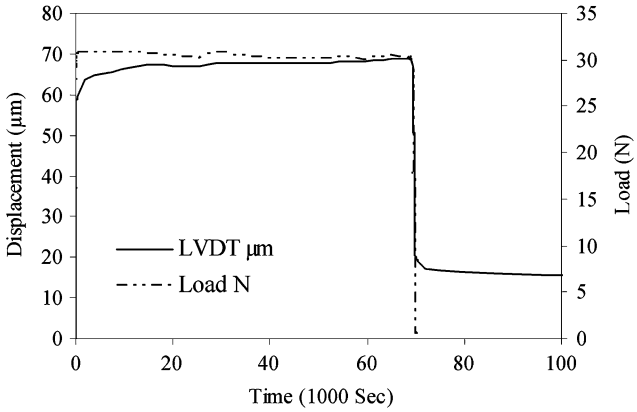

Fig. 11 Displacement and load versus time for Nanox A5 coating at room temperature

for A3, A4, and A8), then it could be concluded that the higher porosity is the reason of showing larger creep stain.

Figure 11 is an evidence of mechanical sliding of splats at room temperature; showing the displacement and load variation based on testing time for a Nanox A5 coating. After loading the sample to about 30 N. The coating shows an immediate elastic deformation but holding the sample under this load at room temperature for about 1 day shows a gradual increase in deformation. Releasing the load did not result in a zero strain, indicating that a permanent deformation has occurred. The mechanical sliding of splats and/or the opening/closing of micro-cracks are likely responsible for this behavior, though the deformation is not significant compared to creep displacements.

3.3 Sintering Effect on Creep Rate

The creep strain versus time graphs show that the creep rate of the zirconia coatings is time dependent. The decrease of creep rate with time can be explained by sintering and microstructure changes in the coating. True

contact area of contact between lamella of thermally sprayed coatings is much smaller than what appears. The early works claimed it as 20% of total area (Fig. 12) (Ref 24); however, later studies using copper electroplating technique showed that by increasing the power of the plasma, the bonding ratio in the deposit could be rapidly saturated to a maximum of 32% for alumina coatings (Ref 25-26).

Small contact area would lead to stress concentration at connected spots, increasing the local driving force for diffusion. Small contact areas mean short paths for cation diffusion as well, which would raise the creep rate at this stage. The higher the local stress, the larger is the creep strain in the primary stage.

Joining of columnar grains and micro-crack healing, explained earlier, restrain splats together and increases the total contact area among them. This leads to an increase of stiffness and increased E. The larger contact area lowers stress concentration and creates longer diffusion paths, both of which reduce strain rate. All the SEM observations and creep test results are consistent with this scenario.

3.4 Sinusoidal Splat Boundaries

In polycrystals, the grain boundaries are regions of relatively weak cohesion, and deformation may occur by the sliding of one grain over another (grain boundary sliding, GBS) (Ref 27-28). It is believed that the rate at which sliding occurs at a stressed grain boundary is determined by the boundary shape, especially when the grain boundary is near 45 degree to the tensile or compression axes where the shear stresses are maximized (Ref 29). At relatively lower temperatures GBS is tied to diffusion mechanisms to accommodate the deformation; otherwise voids will be formed on these boundaries (Ref 30).

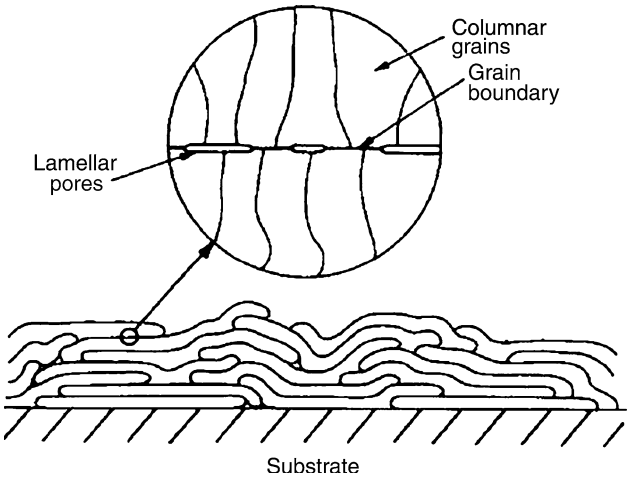

Fig. 12 Schematic representation of the structure of a thermally-sprayed coating (Ref 24)

In thermally sprayed coatings the splat boundaries play a similar role to grain boundaries in monolithic materials—they are interfaces of relatively weak cohesion. Sliding along splat boundaries has frequently been proposed as the primary mechanism of anelastic deformation and creep in thermal spray coatings; as mentioned earlier. In this study a stress exponent of about unity, and relatively low activation energies are consistent with a mechanism involving splat sliding accommodated by diffusion.

One of the challenges in proposing a model based on splat boundaries is how to define them in a model mathematically. The microstructure of thermal spray coatings is rather complicated and consists of splats, non-molten particles, globular pores, and planar voids. Similar difficulties apply to the description of grain boundaries in polycrystalline materials. A great deal of mathematical work has been done in literature to accommodate these grain boundaries into the displacement equations by simplifying the grain boundaries shape to a sinusoidal form accompanied by diffusion mechanisms (Ref 28). Figure 13 illustrates in detail a sinusoidal-shaped boundary showing the wave length and amplitude of the wave and the applied shear stress.

The shape of this boundary could be described simply by:

$$x = \frac{h}{2}\cos\frac{2\pi}{\lambda}y \qquad \text{(Eq 4)}$$

where h is the amplitude and λ is the wavelength. Following the derivation for the sinusoidal grain boundary case, the sliding rate is given as (Ref 28):

$$\dot{\varepsilon} = \frac{8}{\pi}\frac{\tau_{a}\Omega}{kT}\frac{\lambda}{h^2}D_v\left\{1+\frac{\pi\delta D_B}{\lambda\, D_v}\right\} \qquad \text{(Eq 5)}$$

where τ_a is the applied shear stress, Ω the atomic volume, D_V the bulk self-diffusion coefficient, D_B the boundary diffusion coefficient, and δ the thickness of the grain boundary diffusion path. Assuming that the grain boundary

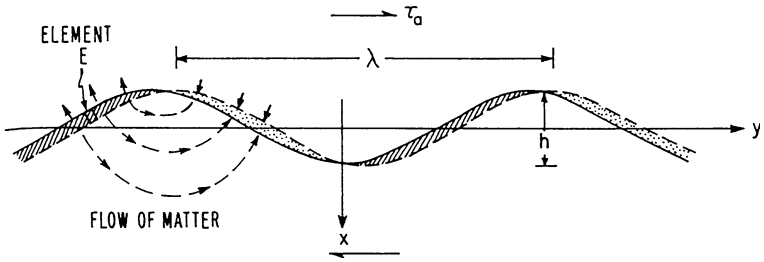

Fig. 13 Grain boundary sliding accommodated by diffusional creep mechanisms in polycrystalline materials (Ref 28)

diffusion coefficient is much larger than that for bulk diffusion, Eq. 5 can be reduced to:

$$\dot{\varepsilon} = 8\frac{\tau_a \Omega \delta}{kT}\frac{D_B}{h^2} \quad \text{(Eq 6)}$$

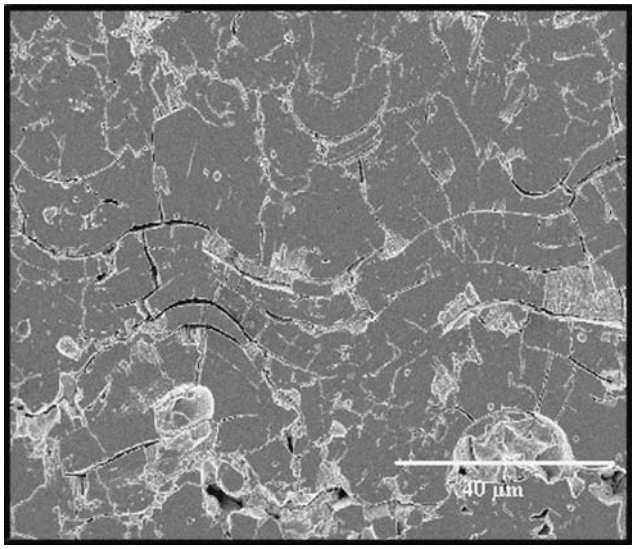

Fig. 14 SEM images of etched Nanox and HOSP coatings showing splat boundaries

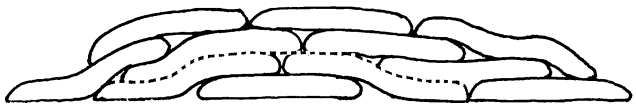

Fig. 15 Coating formation by successive splats overlapping each other; the amplitude of splat boundary wave corresponds to the splat thickness

Considering the formation and final structure of thermally sprayed coatings, this expression could provide a good representation of splat boundaries as well, Figure 14.

3.5 Proposed Model

To use the sinusoidal description of splat boundaries to predict the creep strain and/or rate of thermally sprayed coating the amplitude of the wave must be related to microstructural features of the coating. Considering the formation of a coating to be the accumulation of successive overlapping splats, Fig. 15, the thickness of a splat is a good substitute for h in Eq. 6. Assuming in-plane stresses are linearly proportional to the shear stresses, Eq. 6 can be revised as Eq. 8 to accommodate splat thickness as a coating feature into the equation:

$$\dot{\varepsilon} = B\frac{\Omega \delta D_B}{kT}\frac{\sigma_a}{h_s^2} \quad \text{(Eq 7)}$$

where σ_a is the applied stress, h_s is the average thickness of splats and B is a constant.

3.6 Comparison of Results from the Model and Experiments

Another issue in creep deformation of zirconia is its time dependency, which should be added to the strain rate model, as well. The time dependence has been found to be well described by an equation of the form of Eq. 1 with $s = 0.67$-0.8 (Ref 1, 31-33). In this study a curve was fitted to the all strain versus time graphs of Nanox and HOSP coatings, and resulting value for time exponent was $s = 0.77 \pm 0.02$. Simplifying all the constants into one, the strain equation becomes:

$$\varepsilon = A\frac{\sigma_a}{h_s^2}t^{1-s} \quad \text{(Eq 8)}$$

Employing the splat thicknesses calculated from empirical equations, taking $s = 0.77$, and stress obtained from the

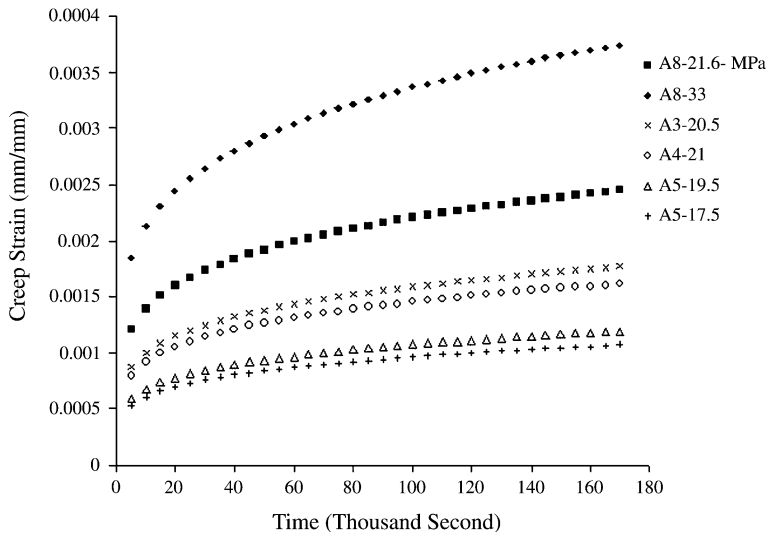

Fig. 16 Calculated creep strain of Nanox and HOSP coatings based on developed model

applied load in each creep test, Eq. 8 was used to calculate strain versus time for 6 samples, and compared with the experimental data, Fig. 16.

The agreement between experimental (Fig. 1) and calculated results for Nanox and HOSP creep strains is very good, though there is a discrepancy for the Nanox A5 coatings. The porosity of this sample is about 18%, more than 6% higher than the other deposits with 11-12% porosity. The level of porosity is not included in Eq. 8, and therefore the higher creep strain of this sample is not predicted.

4. Summary

Different process parameters were used to produce thick, more than 3 mm, plasma-sprayed deposits for creep tests. Creep experiments on PSZ (ZrO_2-7%Y_2O_3) coatings were conducted at 1000 °C under different stress levels. Creep strain graphs plotted for deposits showed higher creep resistance for Nanox samples. The authors recommend that the splat thickness of the plasma-sprayed coatings be considered as one of the important parameters to control the creep strain while all other factors are being kept the same. Increasing splat thickness may lead to a reduction of creep strain/rate especially at primary stage but it will increase conductivity of deposit as well which is not desirable. Therefore, there should be an optimized splat thickness to satisfy creep resistance and thermal diffusivity expected from plasma-sprayed thermal barrier coatings for specific applications.

References

1. D. Zhu and R.A. Miller, Determination of Creep Behaviour of Thermal Barrier Coatings Under Laser Imposed Temperature and Stress Gradients, *J. Mater. Res.*, 1999, **14**(1), p 146-141
2. D. Zhu and R.A. Miller, Sintering and Creep Behaviour of Plasma-Sprayed Zirconia-and Hafnia-Based Thermal Barrier Coatings, *Surf. Coat. Technol.*, 1998, **108-109**, p 114-120
3. E.F. Rfejda, D.F. Socie, and T. Itoh, Deformation Behaviour of Plasma-Sprayed Thick Thermal Barrier Coatings, *Surf. Coat. Technol.*, 1999, **113**, p 218-226
4. A.H. Chokshi, Diffusion Creep in Oxide Ceramics, *J. Eur. Ceram. Soc.*, 2002, **22**, p 2469-2478
5. A.H. Chokshi, Diffusion, Diffusion Creep and Grain Growth Characteristics of Nanocrystalline and Fine-Grained Monoclinic, Tetragonal and Cubic Zirconia, *Scr. Mater.*, 2003, **48**, p 791-796
6. R. Schaller and M. Daraktciev, Mechanical Spectroscopy of Creep Appearance in Fine-Grained Yttria-Stabilized Zirconia, *J. Eur. Ceram.*, 2002, **22**, p 2461-2467
7. M.J. Adnrews, M.K. Ferber, and E. Lara-Curzio, Mechanical Properties of Zirconia-Based Ceramics as Functions of Temperature, *J. Eur. Ceram.*, 2002, **22**, p 2633-2639
8. K. Kokini, Y.R. Takeuchi, and B.D. Choules, Surface Thermal Cracking of Thermal Barrier Coatings Owing to Stress Relaxation: Zirconia vs. Mullite, *Surf. Coat. Technol.*, 1996, **82**, p 77-82
9. L. Vasylkiv, Y. Skka, and V.V. Skorokhod, Low-Temperature Processing and Mechanical Properties of Zirconia and Zirconia-Alumina Nanoceramics, *J. Am. Ceram. Soc.*, 2003, **86**(2), p 299-304
10. M. Daraktchiev and R. Schaller, High-Temperature Mechanical Loss Behaviour of 3 mol% YttriaSstabilized Tetragona Zirconia Polycrystals (3Y-TZP), *J. Phys. Stat. Sol.*, 2003, **2**, p 293-304
11. R. Soltani, T.W. Coyle, and J. Mostaghimi, Thermo-Physical Properties of Bimodal Structured Plasma Sprayed TBCs, *Surf. Coat. Technol.* (accepted Feb 2008)
12. R. Soltani, T.W. Coyle, and J. Mostaghimi, Thermo-Mechanical Behaviour Property of Bimodal Structured Plasma Sprayed TBCs, *J. Am. Ceram. Soc.*, 2007, **90**(9), p 2873-2878
13. W.D. Kingery, H.K. Bowen, and D.R. Uhlmann, Introduction to Ceramics, (2nd ed.). John Wiley & Sons, New York, 1975
14. K.A. Erk, C. Deschaseaux, and R.W. Trice, Grain-Boundary Grooving of Plasma-Sprayed Yttria-Stabilized Zirconia Thermal Barrier Coatings, *J. Am. Ceram. Soc.*, 2006, **89**(5), p 1673-1678
15. J.A. Thompson and T.W. Clyne, The Effect of Heat Treatment on the Stiffness of Zirconia Top Coats in Plasma-Sprayed TBCs, *Acta Mater.*, 2001, **49**, p 1565-1575
16. M.J.M. Akash, Zr Surface Diffusion in Tetragonal Yttria Stabilized Zirconia, *J. Mater. Sci.*, 2000, **35**, p 437-442
17. S. Swaroop, M. Kilo, C. Argirusis, G. Borchardt, and A.H. Chokshi, Lattice and Grain Boundary Diffusion of Cations in 3YTZ Analyzed Using SIMS, *Acta Mater.*, 2005, **53**, p 4975-4985
18. J. Rankin and B.W. Sheldon, In situ TEM Sintering of Nano-Sized ZrO2 Particles, *J. Mater. Sci. Eng.*, 1995, **A204**, p 48-53
19. SHI, Solid State Sintering of Ceramics: Pore Microstructure Models, Densification Equations and Applications, *J. Mater. Sci.*, 1999, **34**, p 3801-3812
20. R.G. Hutchinson, N.A. Fleck, and A.C.F. Cocks, A Sintering Model for Thermal Barrier Coatings, *Acta Mater.*, 2006, **54**, p 1297-1306
21. V. Lughi, V.K. Tolpygo, and D.R. Clarke, Microstructural Aspects of the Sintering of Thermal Barrier Coatings, *Mater. Sci. Eng.*, 2004, **A368**, p 212-221
22. P. Fauchais, M. Fukumoto, A. Vardelle, and M. Vardelle, Knowledge Concerning Splat Formation: An Invited Review, *J. Therm. Spray Technol.*, 2004, **13**(3), p 337-360
23. M. Pasandideh-Fard and J. Mostaghimi, On the Spreading and Solidification of Molten Particles in a Plasma Spray Process: Effect of Thermal Contact Resistance, *Plasma Chem. Plasma Process.*, 1996, **16**(1), p 83S-98S
24. R. McPherson, Thin Solid Films, *Model for the Thermal Conductivity of Plasma-Sprayed Ceramic Coatings*, 1984, **112**(1), p 89-95
25. C.J. Li, Y. He, and A. Ohmori, Characterization of Structure of Thermally Sprayed Coating, *Proceeding of the 15th International Thermal Spray Conference: Meeting the Challenges of the 21st Century*, C. Coddet Ed., May 25-29, 1998 (Nice, France) ASM International
26. C.J. Li and A. Ohmori, Relationships Between the Microstructure and Properties of Thermally Sprayed Deposits, *J. Therm. Spray Technol.*, 2002, **11**(3), p 365-374
27. F.R.N. Nabarro, Creep at Very Low Rates, *Metall. Mater. Trans. A*, 2002, **33A**, p 213-218
28. R. Raj and M.F. Ashby, On Grain Boundary Sliding and Diffusional Creep, *Metall. Trans.*, 1971, **2**, p 1113-1127
29. R.C. Gifkins, Grain-Boundary Participation in High-Temperature Deformation: An Historical Review, *Mater. Charact.*, 1994, **32**, p 59-77
30. M.F. Ashby and R.A. Verrall, Diffusion-Accommodated Flow and Superplasticity, *Acta Metall.*, 1973, **21**, p 149-163
31. H. Echsler, D. Renusch, and M. Schutze, Mechanical Behaviour of as Sprayed and Sintered Air Plasma Sprayed Partially Stabilized Zirconia, *J. Mater. Sci. Technol.*, 2004, **20**, p 869-876
32. T.A. Cruse, B.P. Johnsen, and A. Nagy, Mechanical Properties Testing and Results for Thermal Barrier Coatings, *J. Therm. Spray Technol.*, 1997, **6**(1), p 57-66
33. S.R. Choi, D. Zhu, and R.A. Miller, High Temperature Slow Crack Growth, Fracture Toughness and Room-Temperature Deformation Behavior of Plasma-Sprayed ZrO_2-8 wt.% Y_2O_3, *International Symposium on Advanced Synthesis and Processing, the 22nd Annual Conference on Composites and Advanced Ceramic Materials*, Jan 20-24, 1998, (Cocoa Beach, FL)